Suppression of Zika Virus Infection in the Brain by the Antiretroviral Drug Rilpivirine

Ilker Kudret Sariyer,[1] Jennifer Gordon,[1] Tricia H. Burdo,[1] Hassen S. Wollebo,[1] Eleonora Gianti,[2] Martina Donadoni,[1] Anna Bellizzi,[1] Stephanie Cicalese,[1] Regina Loomis,[1] Jake A. Robinson,[1] Vincenzo Carnevale,[2] Joseph Steiner,[3] Mehmet H. Ozdener,[4] Andrew D. Miller,[5] Shohreh Amini,[1] Michael L. Klein,[2] and Kamel Khalili[1]

[1]Department of Neuroscience, Center for Neurovirology, Lewis Katz School of Medicine at Temple University, 3500 N. Broad Street, Philadelphia, PA 19140, USA; [2]Department of Chemistry, Institute for Computational Molecular Science, College of Science and Technology, Temple University, 1901 N. 12th Street, Philadelphia, PA 19122, USA; [3]Translational Neuroscience Center, National Institute of Neurological Disorders and Stroke, NIH, Bethesda, MD 20892, USA; [4]Monell Chemical Senses Center, 3500 Market Street, Philadelphia, PA 19104, USA; [5]College of Veterinary Medicine, Cornell University, T5-006A Veterinary Research Tower, Ithaca, NY 14853, USA

Zika virus (ZIKV) infection is associated with microcephaly in neonates and Guillain-Barré syndrome in adults. ZIKV produces a class of nonstructural (NS) regulatory proteins that play a critical role in viral transcription and replication, including NS5, which possesses RNA-dependent RNA polymerase (RdRp) activity. Here we demonstrate that rilpivirine (RPV), a non-nucleoside reverse transcriptase inhibitor (NNRTI) used in the treatment of HIV-1 infection, inhibits the enzymatic activity of NS5 and suppresses ZIKV infection and replication in primary human astrocytes. Similarly, other members of the NNRTI family, including etravirine and efavirenz, showed inhibitory effects on viral infection of brain cells. Site-directed mutagenesis identified 14 amino acid residues within the NS5 RdRp domain (AA265-903), which are important for the RPV interaction and the inhibition of NS5 polymerase activity. Administration of RPV to ZIKV-infected interferon-alpha/beta receptor (IFN-A/R) knockout mice improved the clinical outcome and prevented ZIKV-induced mortality. Histopathological examination of the brains from infected animals revealed that RPV reduced ZIKV RNA levels in the hippocampus, frontal cortex, thalamus, and cerebellum. Repurposing of NNRTIs, such as RPV, for the inhibition of ZIKV replication offers a possible therapeutic strategy for the prevention and treatment of ZIKV-associated disease.

INTRODUCTION

Zika virus, also called ZIKV, is an arthropod-borne arbovirus that has captured much attention in recent years due to its global spread by mosquitoes that caused an epidemic and its established association with congenital microcephaly in newborns and Guillian-Barré disease in adults.[1–7] ZIKV is a neurotropic virus that has been repeatedly isolated from newborns with clinical symptoms consistent with ZIKV infection and from brain autopsies of affected individuals.[8–10] While the pathology of the affected brain demonstrates massive neuronal cell injury and dropout, the role of the other cell types, including astrocytes, in supporting propagation of the virus in brain remains to be determined.[11–13]

The genome of ZIKV comprises a single positive-strand RNA of about 10.79 kb in size that, immediately after infection, appears in the cytoplasm and translates into a single polyprotein with a unique long open reading frame (ORF). The ORF encodes for all of the three structural protein genes, including Capsid-C, pre-Membrane-prM, and Envelope-E, from the 5′ regions of the genomic RNA. The 3′ portion of the RNA is responsible for expression of the seven nonstructural protein genes: NS1, NS2A, NS2B, NS3, NS4A, NS4B, and NS5.[14] Replication of ZIKV initiates with the synthesis of a negative-strand RNA that serves as a template for the production of positive-strand RNA. NS5, with its RNA-dependent RNA polymerase (RdRp) activity, is critically important for the production of both positive and negative strands of ZIKV RNA during the infection cycle.[15] In this proof-of-concept study, we provide evidence that a family of non-nucleoside reverse transcriptase inhibitors (NNRTIs), including rilpivirine (RPV), by targeting NS5 strongly suppresses ZIKV replication *in vitro* and alters the preclinical outcome *in vivo* in the ZIKV-infected experimental animals.

RESULTS

Effect of Reverse Transcriptase Inhibitors on ZIKV Infection

As a first step to investigate the biological effect of reverse transcriptase inhibitors on ZIKV, we examined the ability of primary cultures of human fetal and adult astrocytes (PHFAs and PHAAs, respectively) as well as several other cell types, including primary culture of human fetal microglia and fetal neurons (PHFMs and PHFNs, respectively) and human neuroprogenitor cells (NPCs), in supporting ZIKV infection. Results showed a dramatically higher level of ZIKV

A Primary Human Fetal Astrocytes (PHFA)

B Primary Human Adult Astrocytes (PHAA)

strated that RPV has a potential to control ZIKV replication in human brain cell cultures.

Assessment of RPV Binding to ZIKV NS5 via Computation

To gain insight into the mechanism of RPV inhibition of ZIKV replication, first we focused on NS5, an essential viral protein that plays key roles in the life cycle and survival of the virus. The structure of ZIKV NS5 comprises two domains: an N terminus methyltransferase (MTase) domain, responsible for methylation at the viral RNA cap site, and a C terminus RdRp domain, which synthesizes the viral RNA.[16,17] The MTase domain comprises two adjacent binding sites, one for the S-adenosyl-L-methionine (SAM) methyl donor (SAM site) and the other for 7-methyl guanosine diphosphate (^{m7}Gpp) substrate (cap site) (Figure 2; Figures S5 and S6). The RdRp domain features a very large site to accommodate the genome RNA (palm site). The palm site is located at the interfaces of structural features that constitute the hallmarks of the RdRp protein domain, i.e., the palm, fingers, and thumb sub-domains (Figures S5–S8). The majority of the available ZIKV-NS5 structures only comprise either the MTase (apo or bound to substrate/cofactor ligands) or the RdRp domains (apo).

We selected two nearly full-length structures of ZIKV NS5 (PDB: 5TMH and 5TFR),[17,18] and we performed a computational search for druggable sites suitable to accommodate small molecule ligands, including the NNRTI RPV and etravirine (ETR). Our results indicate that the structure of ZIKV NS5 features five potentially druggable sites, suitable for the binding of fragment- or drug-like molecules (Figure 2). In particular, the MTase domain (pink) comprises a druggable spot that extends over both the SAM site and the cap site. Instead, in addition to two small, lateral binding spots, the RdRp domain (light blue) features a very large site, named the palm site, lying in the center of the palm sub-domain.

We explored, by computational docking, the possibility of RPV binding to the top three druggable sites of NS5 (prioritized by considering

infection of PHFAs and PHAAs compared to any other cell types used in this study (Figure S1).

Next, we used these two cell types for further studies, and we observed that, under identical conditions, among the eight distinct members of nucleoside reverse transcriptase inhibitors (NRTIs) and NNRTIs tested in this study, only the NNRTI RPV exhibits a profound ability in suppressing ZIKV infection in both PHFA and PHAA cells (Figure 1). Further studies verified the inhibitory effects of RPV, but not of inhibitors in the NRTI class, including lamivudine (LAM) and abacavir (ABA), on the intracellular level of ZIKV RNA sequences corresponding to NS2A and NS4A genes (Figure S2A). Accordingly, the level of viral capsid protein was found undetectable in the ZIKV-infected cells after treatment with RPV, but not with LAM and ABA (Figure S2B). Moreover, results from western blot analysis revealed a dose-dependent inhibitory effect of RPV on ZIKV production of proteins NS1, NS3, and NS5 (Figures S3A–S3D). Dose effect assessments on naive cells revealed that RPV did not alter cellular viability at up to 25 µM concentrations (Figure S4). Collectively these observations demon-
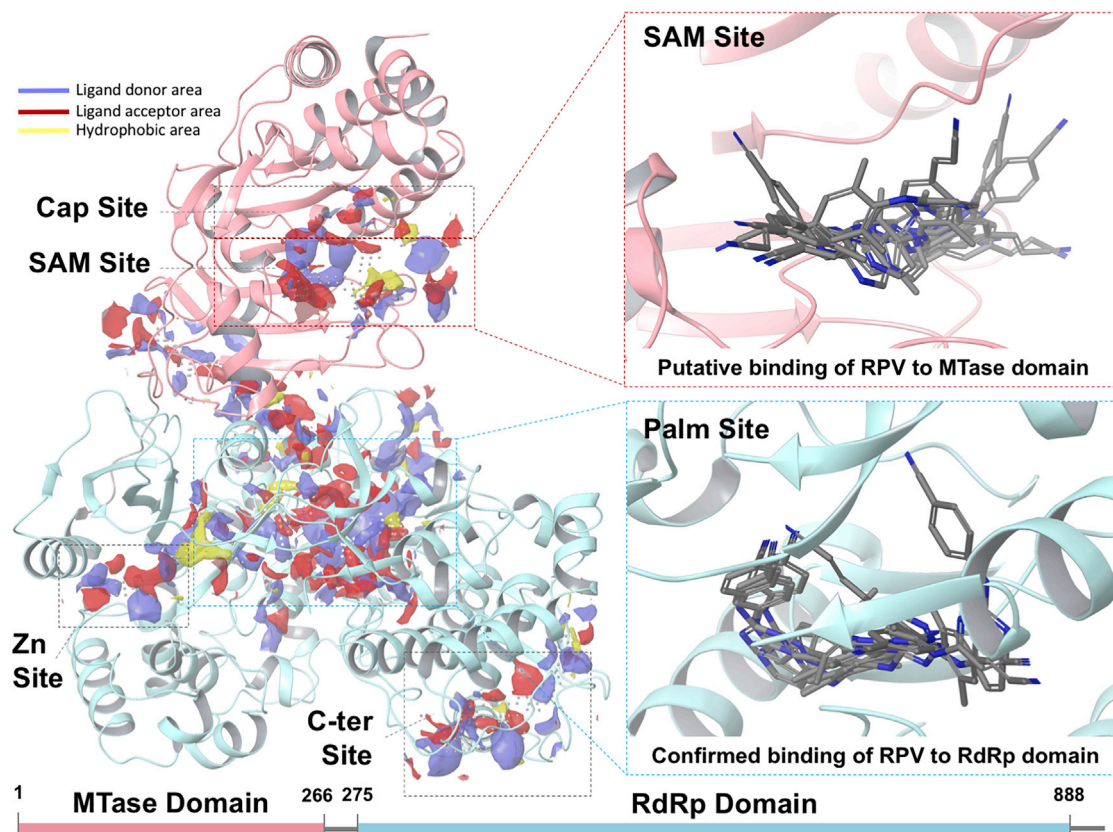
Figure 2. Computational Assessment of RPV Binding to ZIKV NS5

Structural features of ZIKV NS5 and its potential interaction sites with RPV were characterized via computation. The structure of ZIKV NS5 is shown in new cartoon representation. The MTase and RdRp domains are colored in pink and light blue, respectively. Left panel: druggable sites are shown as site maps (yellow, hydrophobic surface; red, ligand acceptor surface; and blue, ligand donor surface). Right panels: zoom-in of the SAM site (top panel) and the palm site (bottom panel). For each site, top scoring binding modes of RPV are shown.

Dscore[19] and by their ability to bind known ligands), namely, the cap site, SAM site (MTase domain), and palm site (RdRp domain). Due to a poor docking score, we promptly excluded the hypothesis that RPV could bind at the cap site. However, docking results alone could not rule out RPV binding to the other two locations, namely, the SAM and the palm sites. Representative binding modes of RPV to NS5 are shown in Figure 2 (right panels). Furthermore, for each site, the best binding modes of RPV are shown in Figures S5–S9. Binding of RPV at the SAM site (MTase domain) superimposed very well with that of the SAM ligand, involving critical residues required for its binding (i.e., H110) (Figure S5). Moreover, RPV overlaps nicely with site maps of complementary chemical features: while the benzonitrile moiety extends over a large hydrophobic area of the receptor (yellow map), the terminal cyanovinyl group points toward the ligand acceptor map (red map).

Binding at the large palm site represented also a viable hypothesis, as suggested by our computational modeling (Figures S6–S9) and partially supported by experimental evidence of HIV-1 reverse transcriptase (RT) structures in complex with RPV and ETR.[20,21] Indeed, both RPV and ETR are known to bind, in a similar fashion as suggested by our modeling, at the palm domain of HIV-1 RT, thereby disrupting the RT polymerase function allosterically. Our computational studies suggested that RPV shows promiscuous binding preferences at the palm site (RdRp domain), with docking poses distributed into three main clusters. In all cases, RPV binds in the proximity of the Priming Loop (PL) feature, but with different orientations: toward the fingers (finger sub-pocket), the palm (palm sub-pocket), or the thumbs (thumb sub-pocket) (Figure S6D). Each binding hypothesis finds experimental counterparts with Dengue virus (DENV) NS5 RdRp structures, apo or co-crystallized with known ligands.[16,22–24] Interestingly, in all three cases, RPV is predicted to adopt a horseshoe-like conformation, typical of RPV binding to HIV-1 RT.[20,21]

Furthermore, in an attempt to predict the bioactive conformations of RPV and ETR, we conducted a search for low-energy conformers of these molecules using a procedure described by Watts et al.[25] As for RPV, our studies predicted two clusters of possible bioactive conformations. The most stable conformers adopted a horseshoe shape, similar to binding modes of RPV in all the sub-pockets at the RdRp

domain and nearly identical to those of the palm sub-pocket at the RdRp domain. Additionally, a second cluster of putative bioactive conformers of RPV was predicted to adopt an extended conformation, similar to that of binding modes at the SAM site (Figure 2; Figure S5). Instead, only one cluster of bioactive conformers was obtained for ETR, which interestingly adopted the horseshoe conformation. Of note, experimental structures of RPV in complex with HIV-1 RT[20,21] indicate that, upon binding, the ligand adopts a conformation, i.e., the horseshoe shape, strikingly similar to our predictions. Taken together, these observations suggested that binding of RPV (and possibly ETR) likely occurs at the palm site (RdRp domain) of NS5. To further corroborate our findings, we computationally selected a set of NS5 amino acid residues, located on the RdRp domain, for experimental mutagenesis and drug-binding studies. These experiments supported the hypothesis that RPV binds at the RdRp domain and ruled out the possibility that binding occurs at the SAM site.

Interplay of RPV with NS5 and Inhibition of ZIKV Replication in Human Brain Cells

To assess interactions of RPV with NS5 protein, we employed differential scanning fluorimetry (DSF) known as protein thermal shift assays.[26–28] We determined that PBS at pH 7.4 (physiologic conditions) usage resulted in reproducible protein melting temperatures (Tm). Upon incubation of NS5-MBP with increasing concentrations of RPV, we observed a concentration-dependent right shift in Tm of about 1°C with 3–10 μM RPV, with an apparent binding affinity of 100 nM (Figure 3A, left). The observed interactions of RPV with NS5 protein were specific to NS5 and not the MBP fusion vehicle, since purified MBP alone exhibited no shift in Tm upon incubation with RPV (Figure 3A, right). Results from the polymerase assay demonstrated that RPV profoundly interfered with the NS5 polymerase activity and, under a similar condition, azidothymidin (AZT), a known NRTI, had no effect on the NS5 activity (Figure 3B). Again, while treatment of the infected cells with AZT had no effects on the ZIKV replication of PHFA, RPV showed a profound inhibitory effect on ZIKV infection of the cells (Figure 3C). Accordingly, computational docking of AZT to the investigated druggable sites of NS5 resulted in a poor predicted binding (Figure S11).

We also evaluated the effect of two other members of NNRTIs that are closely related to RPV, including ETR and efavirenz (EFA),[29] on the ZIKV replication and viral protein production. As shown in Figure 3D, while at 25 μM all three drugs effectively suppressed viral load in the cultured media and inhibited viral capsid production (Figure 3E), the inhibitory effect of RPV and ETR was detected at the lower concentrations of the drugs, a behavior supported by computational investigations (Figures S10 and S11).

To determine the kinetics of ZIKV replication and the effect of RPV on the viral propagation, real-time qRT-PCR was performed. Replication of ZIKV, as determined by the viral RNA copy numbers, was initiated at 1 day post-infection, peaked at day 3, and sharply declined thereafter and remained at very low but detectable levels until day 10

post-infection (Figure 3F). Daily treatment of the infected cells with RPV prevented the burst of the viral replication at day 3 and kept the replication of ZIKV at an undetectable level during the course of our study. Interestingly, interruption of the RPV treatment at day 4 post-infection caused no rebound in the virus production during the remaining course of the 10-day experiment (Figure 3F). This observation rules out the emergence of mutant virus that may escape from the inhibition imposed by RPV. Treatment of the infected cells with various concentrations of RPV that effectively suppressed viral replication improved the cell viability and/or restored cell proliferation (Figure 3G). Examination of viral replication in primary culture of human fetal brain astrocytes by immunocytochemistry showed the presence of NS1 in the cells expressing astrocytic cell marker protein glial fibrillary acidic protein (GFAP) and their absence upon the treatments with RPV, but not AZT (Figures 3H and 3I).

Interaction of RPV with NS5 and Its Effects on Enzymatic Activity

To gain more insight into the RPV binding to NS5 and its impact on polymerase activity of the protein, we selectively mutated 14 amino acid residues to alanine within the palm region of the protein that possesses potential binding affinity to RPV, as predicted by our computational modeling (Figures 4A and 4B; Figures S10 and S11). NS5 mutant proteins were recombinantly synthesized, purified, and utilized for a thermal shift assay and RNA polymerase assays in the presence or absence of RPV. The results did rule out any involvement of MTase domain of NS5, located in the N terminus of the protein, in binding to RPV (Figure 4C). Accordingly, these results confirmed that RNA polymerase activity of wild-type RdRp NS5 (C terminus) is dramatically affected by the presence of RPV (Figure 4D). Interestingly, the mutant construct carrying mutations in 14 amino acid residue positions, as identified by the computational modeling (NS5-RdRp mutant-14A), maintained RNA polymerase activity, although at reduced capacity, when compared to the truncated wild-type protein. In the presence of RPV, RNA polymerase activity was only mildly alleviated, in agreement with RPV-binding affinity studies that detected no binding to the mutated construct. Loss of experimental binding affinity, in conjunction with enzymatic activity at almost full capacity, suggested that one or more amino acid residues mutated in the 14A construct are critical for RPV binding.

Binding affinity of AZT to the RdRp-wild-type (WT) and RdRp mutant domains was also analyzed by thermal shift assay, and the results indicated that the Tm was not changed in a concentration-dependent manner, so no significant binding of AZT to these proteins was observed (data not shown).

To further determine and characterize selective anti-ZIKV activity of RPV, we utilized the RdRp-14A protein, which showed a comparable polymerase activity but no significant binding to RPV. RdRp-14A was cloned into a mammalian expression vector and transiently transfected into primary human astrocytes. The cells were then infected with ZIKV in the presence and absence of RPV and analyzed by qRT-PCR for viral replication. As expected, ZIKV infection was
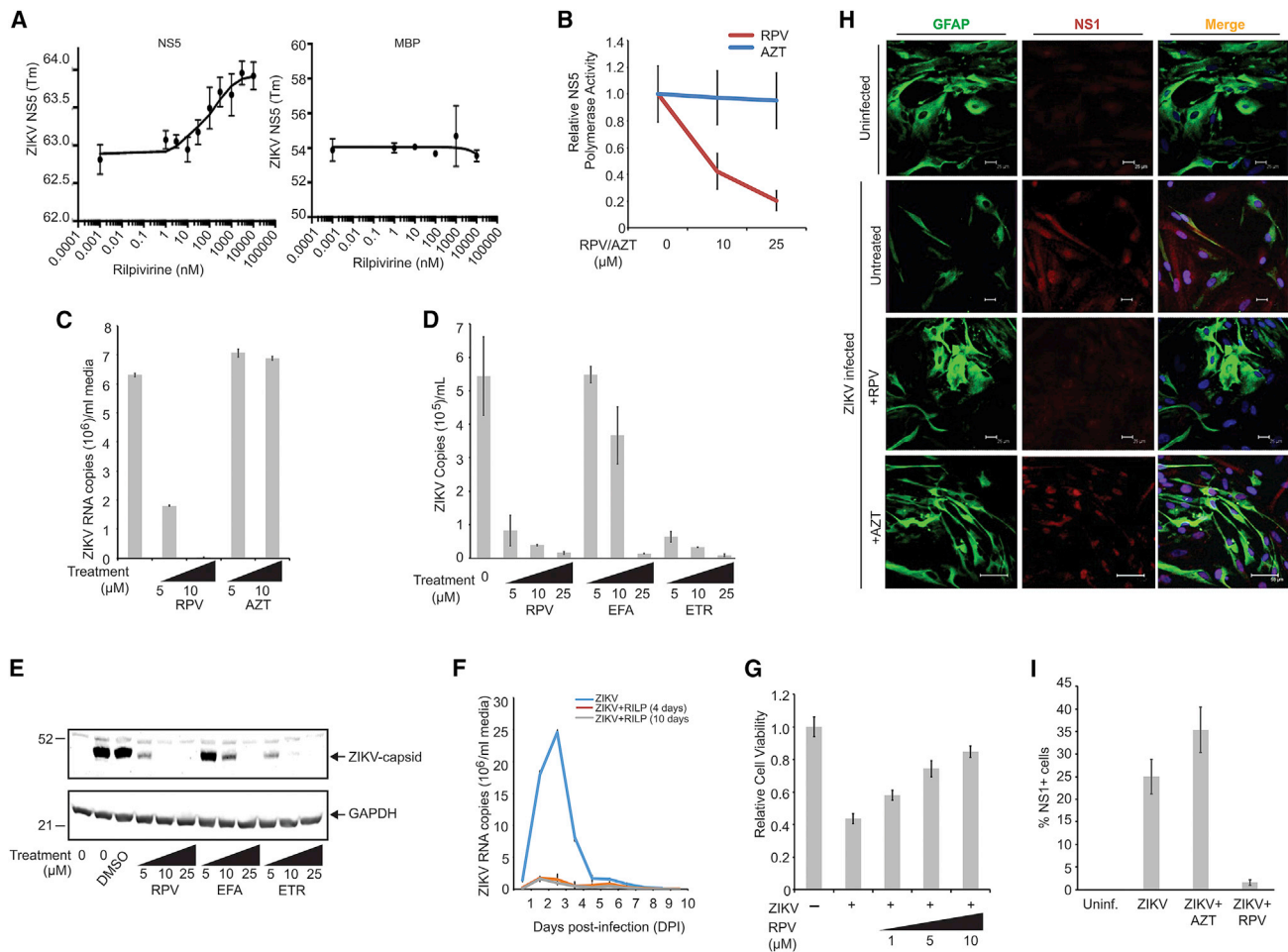
Figure 3. Inhibition of ZIKV Infection of Human Primary Culture of Brain Cells by RPV

(A) Interaction of ZIKV NS5 protein with RPV using protein thermal shift assays. The relative fluorescence emitted by the thermal shift dye is recorded during the temperature ramp phase and plotted versus temperature (left panel). Tm value was calculated from the derivative of the thermal melt curves and plotted as effects of various concentrations of RPV, as described in the Materials and Methods. Determination of binding interaction of maltose binding protein (MBP) moiety of NS5-MBP with RPV using differential scanning fluorimetry (DSF) showed no association of MBP with RPV (right panel). (B) RPV inhibits RNA polymerase activity of ZIKV NS5 protein. 1 μg ZIKV RNA and 500 ng recombinant NS5 protein were added to the reaction buffer, in the presence and absence of RPV or AZT at 10- or 25-ng concentration, and analyzed as described in the Materials and Methods. Relative NS5 activity was calculated from three independent experiments and is shown as a trend-line graph. (C) PHFA cells were infected with ZIKV (0.5 plaque-forming unit [PFU]). Cells were treated daily with increasing concentrations of RPV and AZT (5 and 10 μg/mL). At 3 dpi, ZIKV RNA copies in the growth media were analyzed by real time qRT-PCR and are shown as a bar graph. (D) PHFA cells were infected with ZIKV (0.1 PFU). Cells were treated daily with increasing concentrations of RPV, EFA, and ETR (5, 10, and 25 μg/mL). At 3 dpi, ZIKV RNA copies in the growth media were analyzed by real time qRT-PCR and are shown as a bar graph. (E) Whole-cell protein extracts were also prepared from the same set of experiments from (D) and analyzed by western blotting for the detection of ZIKV capsid protein. GAPDH (glyceraldehyde-3-phosphate dehydrogenase) was probed in the same membranes and is shown as a loading control. (F) PHFA cells were divided into three groups. The first group was infected with ZIKV and mock treated at 24-h intervals for 10 days. The second group of cells was infected with ZIKV (0.1 PFU) and treated with RPV (5 μg/mL) at 24-h intervals for only 4 days. The third group was also infected with ZIKV (0.1 PFU) and treated with RPV (5 μg/mL) at 24-h intervals for 10 days. The growth media of cells were collected every day, starting from 1 dpi up to 10 dpi, and analyzed by real time qRT-PCR. ZIKV viral loads were determined as ZIKV RNA copies per milliliter culture media and are shown as a trend-line graph for each group. (G) PHFAs were infected with ZIKV (0.1 PFU) and treated with RPV at 1-, 5-, and 10-μg/mL concentrations for 4 days. PHFA cell viability was analyzed by MTT (3-(4,5-dimethylthiazol-2-yl)-2,5-diphenyltetrazolium bromide) assay and is shown as a bar graph from three independent experiments. (H) PHFA cells were infected with ZIKV (0.1 PFU) and treated daily with RPV and AZT. At 4 dpi, cells were fixed and processed by immunocytochemistry for the detection of cellular GFAP (green) and viral NS1 (red) proteins, as described in the Materials and Methods. (I) DAPI-positive and NS1-immunoreactive cells from studies shown in (H) were counted in at least three different stainings of the conditions using Photoshop, and percentages of NS1 cells were graphed.

greatly suppressed by RPV in control infections. On the other hand, co-expression of the RdRp-14A protein in ZIKV-infected cells was able to recover RPV-mediated suppression of ZIKV replication (Figure 4E). These results further suggest that RdRp-14A mutant is enzymatically active in cells and able to complement the RPV-mediated suppression of the wild-type RdRp functions.
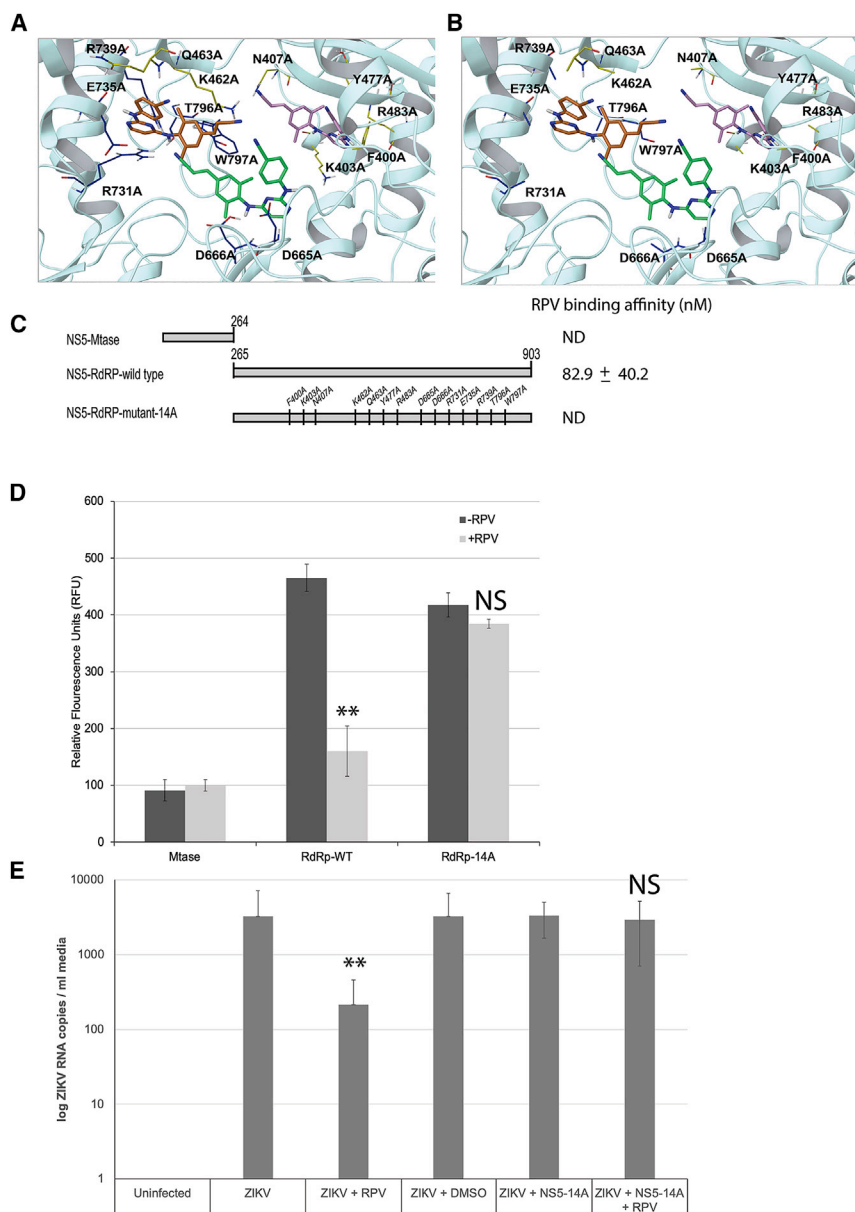
Figure 4. Physical and Functional Assessment of RPV Binding to NS5 Mutants with Site-Directed Mutagenesis

Structural features of ZIKV NS5-RdRp wild-type (A) and NS5-RdRp mutant-14A (B) and their potential interaction with RPV were characterized via computation. In both wild-type (A) and mutant-14A (B) panels, side chains are color coded by NS5 mutant (yellow or blue for mutant-N7A or mutant-C7A, respectively). Binding modes are ranked by docking score (kcal/mol): −7.4 (best predicted binding), −6.6, and −5.6 for RPV poses in green, orange, and pink carbons, respectively. The bottom ranking pose (pink carbons) is obtained for RPV interacting with mutant-N7 residues and shows no binding; hence, this binding mode (pink carbon RPV) is less likely to occur. (C) Schematic presentation of amino acid mapping of NS5 wild-type and side-directed mutations (14A) are illustrated. The relative fluorescein emitted by the thermal shift dye is recorded during the temperature ramp phase and plotted versus temperature. ND denotes no significant affinity detection. (D) Effect of RPV on RNA polymerase activities of MTase domain and RdRp wild-type and RdRp-14A proteins was also analyzed by RdRp assay. 1 μg ZIKV RNA and 500 ng recombinant NS5 full-length or mutant proteins were added to the reaction buffer in the presence and absence of RPV (10 ng) and analyzed as described in the Materials and Methods. NS5 activity was calculated from three independent experiments and quantified as relative fluorescence units (RFU) emitted during the reaction. (E) ZIKV RdRp-14A mutant was cloned into a mammalian expression vector. PHFA cells were transiently transfected with this construct and either treated with RPV or left untreated. Cells were infected with ZIKV (0.1 PFU) at 24 h post-transfections, and growth media of cells were analyzed by qRT-PCR for ZIKV RNA copies. **p < 0.05.

RPV Suppresses ZIKV Infection in IFN$^{-/-}$ Mice and Changes the Preclinical Outcome

To extend our *in vitro* results, we established an *in vivo* mouse model of ZIKV infection. Interferon receptor (IFNR)-knockout (IFNR$^{-/-}$) mice (n = 6) were infected with the Puerto Rico (PRVABC59) strain of ZIKV through footpad injections.[30] Three of these animals were also treated with RPV (ZIKV + RPV) in order to explore the utility of RPV as an anti-viral agent for ZIKV *in vivo*. The control group was uninfected mice treated with RPV (uninfected RPV only, n = 3). In a second set of experiments, results from these studies were validated using a larger cohort of animals in each group (n = 6; Figure S12). All mice were monitored daily for survival and signs of disease with bi-daily weight monitoring and daily grasp test analysis. Physical, behavioral, and motor coordination/paralysis inspections were also performed at the time of weight checks bi-daily.

Both sets of ZIKV-infected animals lost weight (Figures 5A and S12A); however, the RPV-treated ZIKV-infected animals recovered. There was no significant weight loss in the RPV-only animals. Clinical scores (as measured by grasp test and physical assessment) in ZIKV-infected animals were increased after infection. The animals treated with RPV returned to baseline levels where the untreated animals continued to progress with poor clinical scores (Figure 5B; Figure S12B). Mice were sacrificed based on weight loss and physical, behavioral, and motor function deficits. One ZIKV-infected animal was sacrificed at 7 days post-infection (dpi) and two others at 8 dpi, suggesting that ZIKV infection is highly lethal in IFNR$^{-/-}$ mice (Figure 5C). In the second set of studies, all six ZIKV-infected animals were sacrificed at 8 dpi (Figure S12C). On the other hand, all mice from ZIKV-infected and RPV-treated groups survived until
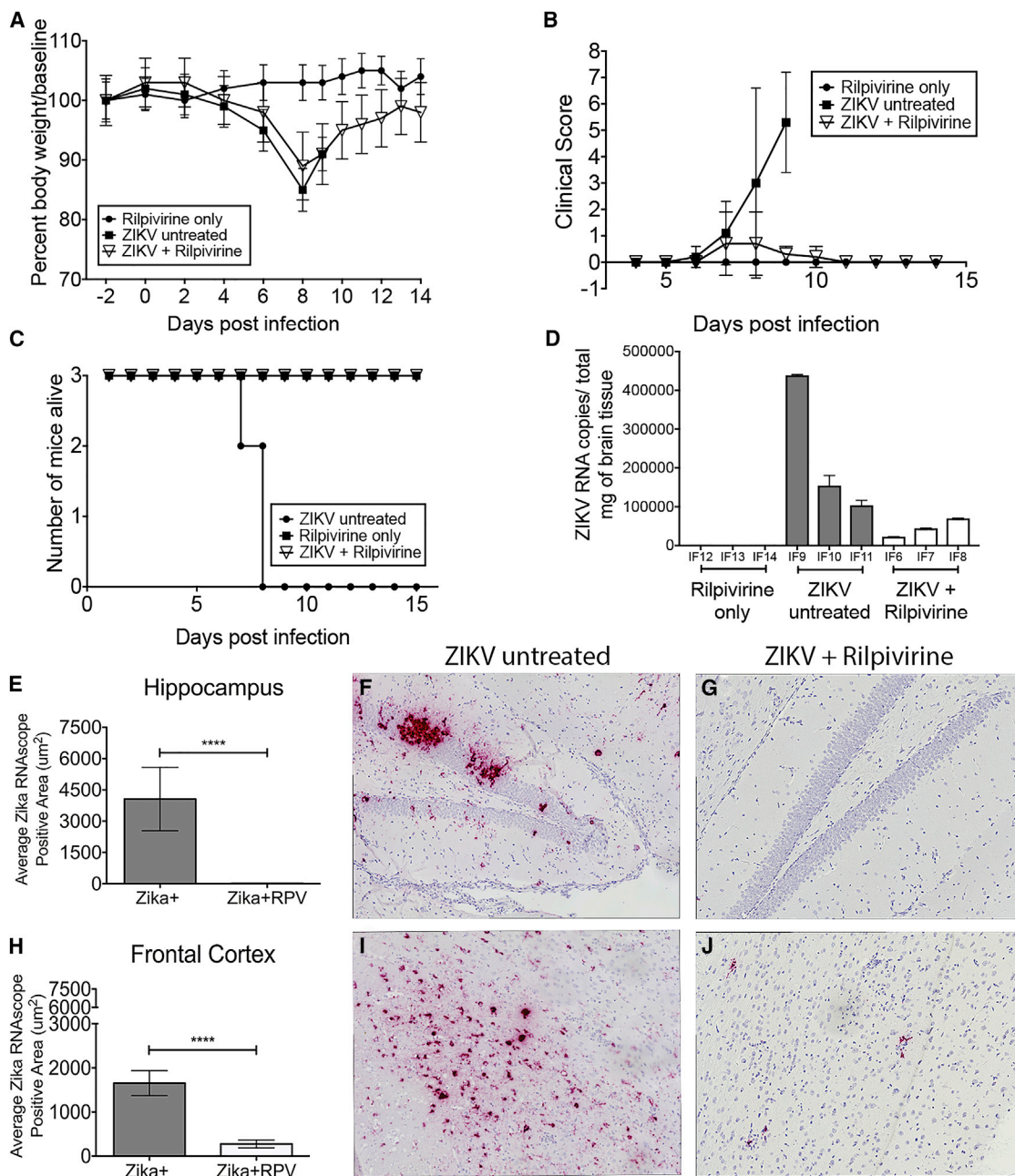
Figure 5. RPV Inhibits ZIKV Propagation, Reverses the Mortality, and Decreases the Viral Burden in the Brain of IFNR$^{-/-}$ Mice

(A) Body weights were measured for each mouse from the three groups (closed circle, rilpivirine only; closed square, ZIKV untreated; and open triangle, ZIKV + RPV) until the end of the study (14 days post-infection [dpi]). Data are shown as a percent of body weight compared to baseline. (B) Grasp tests were performed daily starting at 4 dpi and analyzed for clinical scoring for the three groups. (C) Survivor curve analysis is shown based on the Kaplan-Meier estimates. All animals in the uninfected + RPV and ZIKV-infected + RPV groups survived until the end of the study. The ZIKV-infected and untreated mice were sacrificed at 7 and 8 dpi. (D) ZIKV RNA copies per milligram total brain lysates are presented per animal (IF6–IF14). The mean and SD are shown, and the SD was calculated from triplicate analysis of the RNA samples from each mouse. (E–J) ZIKV RNA was visualized with RNAscope (red) and quantified in the hippocampus and the frontal cortex of ZIKV-infected untreated animals (ZIKV+) and ZIKV-, RPV-treated animals (ZIKV + RPV). (E) The average ZIKV+ RNA area in the hippocampus of the ZIKV-untreated (gray bars) mice compared to the ZIKV + RPV group (white bars) showed a significant reduction in the ZIKV RNA with RPV (p < 0.0001). (F) Representative image of hippocampus ZIKV RNAScope staining reveals high viral RNA signal in ZIKV mice. (G) Representative image of hippocampus ZIKV RNAScope staining shows significantly less signal in ZIKV + RPV mice. (H) The average ZIKV+ RNA area in the frontal cortex of the ZIKV-untreated (gray bars) mice compared to the ZIKV + RPV group (white bars) showed a significant reduction in the ZIKV RNA with RPV (p < 0.0001). (I) Representative

(legend continued on next page)

the end of the study (14 dpi), suggesting that RPV was capable of reversing ZIKV-associated mortality in this animal model.

At the end of the study, brain and peripheral organs (spleen, liver, kidney, and lung) were harvested for pathological analysis at necropsy. All brain regions (thalamus, hippocampus, frontal cortex, and cerebellum) examined in the ZIKV-only mice had significant inflammation, but also abundant apoptotic/necrotic cell damage, which has been described in other ZIKV-infected mouse models.[30–32] In the RPV-treated ZIKV-infected animals, there was still significant inflammation, but no apoptotic/necrotic cell damage was observed (Figure S13). The RPV-only control brains were unremarkable. Spleen, liver, kidney, and lung from all mice were unremarkable with no pathology (Figure S14).

ZIKV RNA copies in post-mortem brain were quantified in all animals by RT-PCR (Figure 5D). As expected, there were no ZIKV RNA copies detected in the RPV-only control animals. There were up to 400,000 copies of ZIKV RNA/mg of tissue detectable in the infected animals. The ZIKV RNA copies in the brain were significantly reduced in mice treated with RPV. To assess viremia in the specific regions of the brain of ZIKV mice, we utilized an RNAscope to detect Zika viral RNA in hippocampus and frontal cortex (Figures 5E–5J). The kidney, liver, lung (Figures S14A–S14F), spleen (Figures S14G–S14I), thalamus (Figures S14J–S14L), and cerebellum (Figures S14M–S14O) were also assessed for ZIKV RNA. Administration of RPV significantly decreased the amount of ZIKV RNA$^+$ cells in the hippocampus compared to ZIKV only (Figures 5E–5G; 4,061.5 ± 1,515.1 μm^2 versus 25.5 ± 12.4 μm^2, p < 0.0001). Similarly, in the frontal cortex there was a significant reduction in ZIKV RNA in mice treated with RPV (Figures 5H–5J; 1,653.3 ± 283.0 μm^2 versus 273.0 ± 89.0 μm^2, p < 0.0001). A significant decrease in ZIKV RNA was seen in the spleen, thalamus, and cerebellum (Figures S14G–S14O). There was very little to no virus seen in the kidney, liver, and lung (Figures S14A–S14F). Overall, RPV administration proved efficacious at preventing ZIKV infection in the brain, with a dramatic reduction of ZIKV RNA in the brain and spleen.

The *in vitro* data presented thus far have demonstrated ZIKV replication predominantly in astrocytes. To examine the specific CNS cell types infected by ZIKV *in vivo*, dual RNAscope for ZIKV RNA and subsequent immunohistochemistry for cell subpopulations were utilized. Co-localization was investigated in the hippocampus and frontal cortex preferentially due to the higher viral RNA in these two regions with ZIKV infection. As demonstrated *in vitro*, ZIKV RNA showed overlap with GFAP+ astrocytes in both the frontal cortex and hippocampus (Figures 6A and 6B). Virus was detected in both the cell body and in the astrocytic projections. Microglia and macrophages were detected using an antibody against IBA-1 and showed

significant co-localization with ZIKV RNA (Figures 6C and 6D). T cell accumulation, visualized by CD3, in the brains of ZIKV-infected mice was noted compared to uninfected controls (data not shown). ZIKV RNA was detected in T cells in both the frontal cortex and the hippocampus (Figures 6E and 6F). Viral RNA showed co-localization with neurons in the frontal cortex, but, in the hippocampus, NeuN and viral RNA showed more proximity than overlap (Figures 6G and 6H). An antibody against nestin was used to examine the presence of progenitor cells in the frontal cortex and hippocampus. There were no nestin+ cells detected that contained ZIKV RNA (Figures 6I and 6J). Overall, these *in vivo* results show that the major cell populations infected in this model are astrocytes, inflammatory monocytes, and T cells and neurons.

DISCUSSION

Through a computational assessment of ZIKV NS5, we identified potential sites of interaction with the NNRT inhibitor RPV that may impact on the enzymatic activity of NS5, hence impairing a productive ZIKV infection cycle. In particular, we showed that NS5 features two druggable sites, both suitable for the binding of small molecule ligands, like RPV. The first one, the SAM site, is located on the MTase domain of NS5 (N terminus), and coincides with the binding pocket of SAM, the methyl donor in the 5′ RNA cap structure.[16] Therefore, the binding at this site of small molecules, such as RPV and ETR, would compromise allosterically viral replication. The second site, the palm site, is located on the RdRp domain of NS5 (C terminus) and overlaps with a ligand-binding pocket shared by DENV NS5 and conserved within the flavivirus family.[24] It has been shown that competitive binding at the palm site inhibits enzymatic activity of DENV RdRp.[24] We envision that a similar mechanism might be exerted by the binding of RPV (as well as by other NNRTIs, like ETR) at equivalent locations in ZIKV NS5.

Further studies, including the computationally guided experimental mutation of several amino acid residues with potential binding affinity for RPV, excluded the hypothesis that the MTase domain of NS5 (N terminus) is involved in binding to RPV. On the contrary, we found that RPV has an affinity for binding to the RdRp domain (AA265-903 strain) of the NS5 protein (C terminus). Interestingly, by introducing mutations of 14 amino acid residues (mutant-14A), as suggested by computational modeling, we showed that RPV interactions with the RdRp domain are significantly alleviated, a clear indication that RPV binding is mediated by one or more of the mutated residues. In addition, the results from the polymerase activity assay further corroborated with binding data, thereby suggesting that RPV interferes with NS5 polymerase activity by binding to its RdRp domain. Further computational work (i.e., extensive molecular dynamics simulations), combined with experimental mutagenesis and *in vitro* activity studies, will be required to characterize the

---

image of a frontal cortex ZIKV RNAScope *in situ* reveals high viral RNA signal in ZIKV mice. (J) Representative image of frontal cortex ZIKV RNAScope staining shows significantly less signal in ZIKV + RPV mice. The average ZIKV RNA signal area was quantitated as the average of 10, non-overlapping 40× images from each animal (n = 3/group), using a Keyence BZ-X700 microscope. Bar graphs show average ZIKV RNA area (mean, SEM). Comparison of means was determined by Mann-Whitney, two-tailed t test (*p < 0.05, ****p < 0.0001).
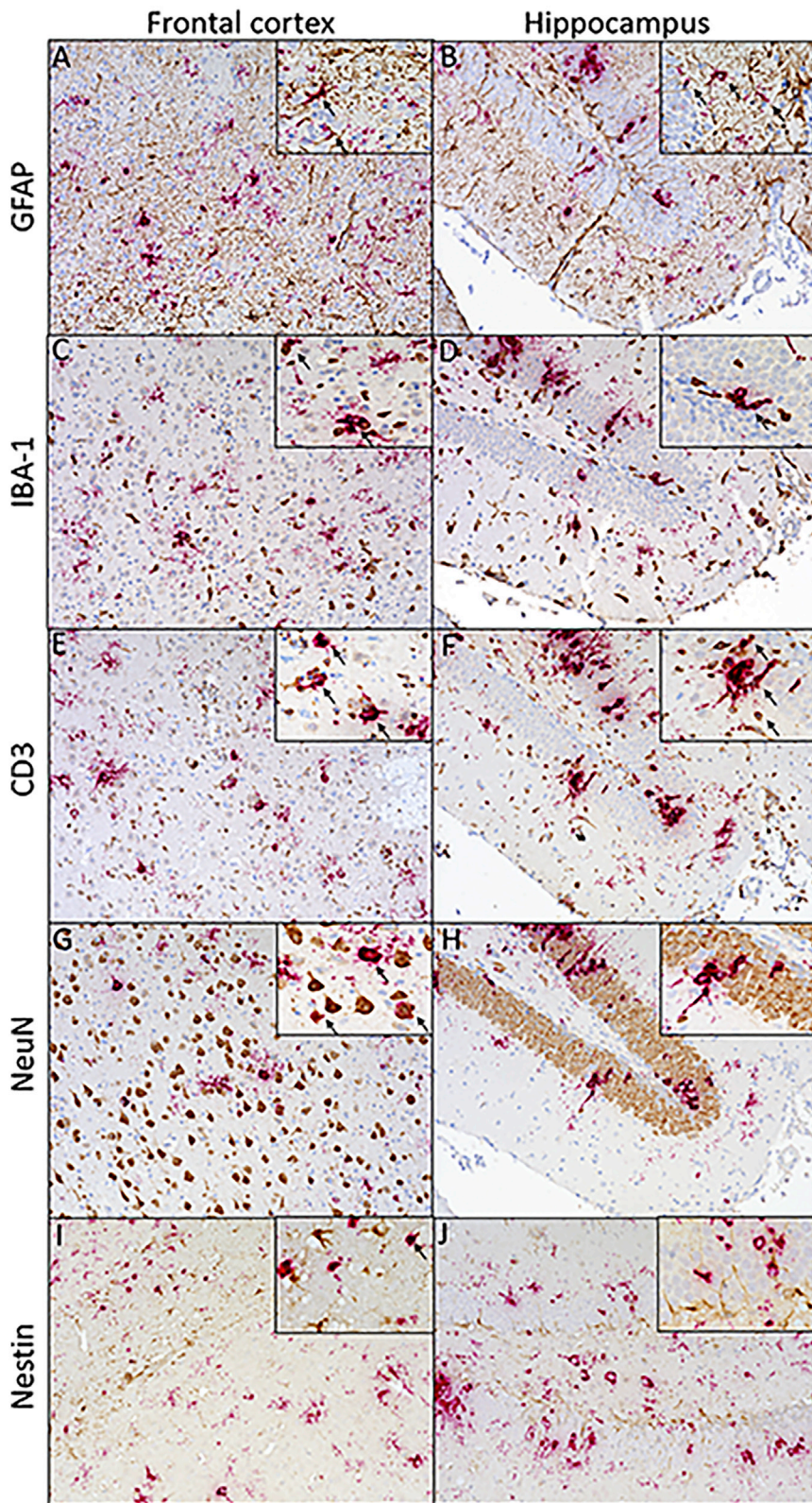
Figure 6. ZIKV RNA Co-localization with Astrocytes and Microglia/Macrophages

T cells, neurons, and progenitor cells in the frontal cortex and hippocampus. ZIKV RNA was visualized with RNAscope (red) and cell markers by immunohistochemistry (brown) in the frontal cortex and hippocampus of ZIKV-infected animals (ZIKV+). GFAP was used to visualize astrocytes in tissue. Astrocytes showed significant overlap with viral RNA in the frontal cortex and hippocampus. (A and B) IBA-1 served as a marker for microglia and macrophages in tissue. Microglia and macrophages showed co-localization with viral RNA both in the frontal cortex (A) as well as the hippocampus (B). (C and D) CD3 was used to characterize T cells in tissue, which showed co-localization with viral RNA in the frontal cortex (C) and the hippocampus (D). (E and F) Neuronal nuclear protein, NeuN, served as a marker for neurons in tissue. Viral RNA showed co-localization with neurons in the frontal cortex (E), but, in the hippocampus (F), NeuN and viral RNA showed more proximity than overlap. (G and H) No overlap of staining is seen with ZIKV RNA and nestin, a marker of progenitor cells: frontal cortex (G) and hippocampus (H). (I and J) Representative images were taken at 20× magnification with a Keyence BZ-X700 microscope: frontal cortex (I) and hippocampus (J). Magnified images were taken at 60× and arrows were used to denote double-positive cells.

structural details of the conformational transitions associated with ZIKV polymerase activity (so far largely unknown) and to fully elucidate the binding preferences of NNTIs to NS5, starting with RPV and ETR. Nonetheless, our current work offers a proof of concept that RPV can bind to ZIKV NS5, resulting in severe impairment of its activity, as shown in our study and viral RNA genome replication in a well-controlled cell culture model. Besides characterizing the presence of multiple druggable hotspots of ZIKV NS5 (both at the MTase and RdRp domains) that can be targeted by small molecule modulators, our studies, by highlighting the role played by the intrinsic plasticity of ZIKV NS5 into small molecule ligand binding, emphasize the importance of incorporating protein flexibility into drug discovery strategies.

To assess the *in vivo* impact of RPV on ZIKV infection, we then employed the IFN$^{-/-}$ mouse model that has been widely used to demonstrate ZIKV replication in brain.[30] All brain regions (thalamus, hippocampus, frontal cortex, and cerebellum) examined in the ZIKV-infected mice had significant inflammation, but also abundant apoptotic/necrotic cell damage, which has been described in other ZIKV-infected mouse models.[31] The brains of the ZIKV-infected animals had high levels of ZIKV RNA detected both by RT-PCR and RNAScope. *In vivo*, in ZIKV-infected mice, we detected predominantly ZIKV-infected astrocytes, activated microglia and macrophages, T cells, and neurons by dual ZIKV RNAScope followed by immunohistochemistry. Interestingly, very little to no nestin-1+ neuroprogenitors were infected *in vivo*. Supporting our findings is a recent study describing ZIKV widely infecting the astrocytes and neurons of adult AG129 mice.[32] Spleen, liver, kidney, and lung from all mice were unremarkable without any pathology, and little virus was detected in the spleens of ZIKV animals. Thus, pathology in the ZIKV infection in IFN$^{-/-}$ mice delivered by footpad injection, a physiological route of infection, seems to be highly neurotropic and restricted to brain and not peripheral organs.

In a small animal model of ZIKV disease, we demonstrated that RPV suppressed viral replication, decreased brain inflammation, protected neurons from apoptosis and necrosis, and reversed ZIKV-associated mortality. In the RPV-treated ZIKV-infected animals, there was still significant inflammation in the brain, but no apoptotic/necrotic cell damage was detected, which corresponded to the reversal of mortality. Our findings further indicate that RPV is efficacious at inhibiting ZIKV viral infection in the brain and spleen. Our data would suggest that RPV functions by binding NS5 and, thereby, impacting the enzymatic activity of this viral protein and the productive ZIKV infection cycle.

We recognize that, in the IFN-null context, mice lack all IFN signaling and IFN anti-viral responses, thus succumbing to ZIKV infection with high viral load in brain, with evidence of neurologic disease.[30] However, the fact that RPV can reverse the severe detrimental effects of ZIKV infection in these animals is particularly interesting, and it indicates that direct interaction of RPV with the critically important NS5 viral protein has a negative impact on the *in vivo* propagation of ZIKV in the brain. ZIKV has the inability to cause disease in IFN-competent mice, despite the lethality in the IFN$^{-/-}$ mice. This may be linked to the inability of ZIKV to antagonize mouse IFN responses, unlike in humans. A recent study demonstrated that ZIKV NS5 results in proteasomal degradation of IFN-regulated transcription activator STAT2 in human, but not in mice, possibly explaining the requirement in mice for IFN deficiency.[33] It is possible that the interaction of RPV with NS5 could trigger the proteasomal degradation of STAT2 in the absence of IFN.

Since RPV is a commonly used NNRTI in HIV-infected patients, it would be of interest to see if people with HIV who are treated with RPV are at a lower risk for ZIKV infection. In addition, future studies will include *in vivo* studies utilizing other NNRTIs that were found to be suppressive *in vitro*, including efavirenz and ETR.

MATERIALS AND METHODS
Ethics Statement
All samples were obtained and utilized in accordance with Temple University Human Subjects Protections and the approval of the Institutional Review Board (IRB) and Institutional Animal Care & Use Committee (IACUC).

Computational Evaluation of RPV/NS5 Interaction Sites
Protein Structure Selection, Preparation, and Analysis
We first conducted a survey of available experimental structures of ZIKV NS5, including 20 PDB entries (PDB: 5TMH,[15,17] 5TFR,[18] 5VIM,[34] 5GP1, 5GOZ[35] 5WZ1, 5WZ2, 5WZ3,[16] 5KQR, 5KQS,[36] 5NJU, 5NJV,[37] 5ULP,[38] 5WXB,[39] 5UOB, 5UOC,[40] 5U04,[41] 5M5B,[42] 5M2X, and 6I7P[43]) (https://www.rcsb.org/). All these structures were solved by X-ray diffraction, at resolutions ranging between 1.33 and 3.28 Å. Most of them only comprised one of the two NS5 domains, i.e., MTase and RdRp. We prepared all the collected structures by using the protein preparation Wizard,[44] which included the addition of missing hydrogen atoms, removal of water molecules, and structural integrity check (bond-orders and formal charges) of all protein and ligand atoms. Possible missing side chains were reconstructed using Prime,[45] and protonation states were assigned at pH 7; structure relaxation was performed by restrained minimizations with the OPLS3[46] force field (0.30 Å root-mean-square deviation [RMSD] heavy atom convergence). We then superimposed all NS5 structures onto a common reference template to enable structural comparisons. We finally selected two structures of NS5 (PDB: 5TMH and 5TFR),[17,18] each comprising both domains, for further computational studies. Additionally, we included in our study a number of DENV NS5 structures that were used to refine our computational docking model at the palm site (RdRp domain) (analyzed NS5 DENV structures PDB: 5HMW, 5HMX, 5HMY, 5HMZ, 5HN0, 5I3P, 5JJR, 5I3Q, 5JJS, 5K5M,[22] and 3VWS[23]). All DENV NS5 structures were subject to the outlined protein preparation procedure.

Binding Site Detection
To identify putative sites of NS5 suitable for ligand binding, we used a procedure similar to what we implemented elsewhere.[47] In brief, we

used SiteMap,[19] and sites were detected by applying a standard grid and a more restrictive definition of hydrophobicity. Maps were cropped at 4 Å from the nearest site point.

Ligand Preparation
We prepared a number of ligand structures, including RPV, ETR, and AZT, as well as ligands extracted from co-crystal complexes of NS5 proteins from ZIKV and DENV. All ligands were prepared using the standard LigPrep procedure,[48] with Epik[49] for attributing protonation states and predicting pKa values.

Molecular Docking by Rigid Receptor
We performed molecular docking[50] of RPV and the other ligands against the NS5 protein of ZIKV (PDB: 5TMH).[17] Docking was performed by rigid receptor at the SP level. An exhaustive series of grids was used to define the space for ligand docking. First, we used individual site maps to center the docking space on putative druggable sites detected by SiteMap. Then, for the MTase domain, we used the ligands co-crystallized at the SAM site or the cap site of NS5 (SAH and ^{m7}Gpp; PDB: 5TMH and 5KQS, respectively)[17,36] to define the docking space. Instead, for the RdRp domain, we extracted fragment ligands from DENV NS5[22] that were placed at equivalent locations of ZIKV NS5 (upon superimposition of ZIKV and DENV NS5 structures, followed by relaxation by minimization). These fragment ligands were then used to center the docking grids on the NS5 palm site. For each investigated site, top scoring binding modes of RPV were selected.

Induced-Fit Docking
We selected the most promising binding modes of RILP and ETR at both the SAM site and the palm site for additional refinements by induced-fit docking (IFD).[51] During IFD, docking space was defined by the centroids of rigid-docking ligands, and the SP scoring function was used. To treat the receptor flexibly, all residues within 5 Å of a ligand were refined and optimized using the OPLS3 force field.

Conformational Search
We used ConfGen[25] to perform searches for bioactive conformations of RPV and ETR. During our calculations, we used the OPLS3 force field to perform minimizations; to eliminate redundant conformations, we used a 0.5-Å RMSD cutoff with energy window of 120 kcal/mol.

Computational Prediction of NS5 Mutants
We initially used the structures of NS5 bound to RPV and ETR, as predicted by computational docking, to systematically scan and mutate amino acid residues critical for binding at either the MTase domain (SAM site) or the RdRp domain (palm site). We performed amino acid mutations within the Schrödinger computational suite;[48] upon each mutation, we performed a short minimization to relax the structures around mutant residues and their local structural neighbors. Whenever necessary, we ran a full restrained minimization of the complex to re-optimize the H-bond networks. After excluding that the binding of RPV may occur at the MTase domain (by NS5-

MTase truncation followed by site-directed mutagenesis studies and binding affinity predictions; Figure 3A), we visually inspected all mutant complexes at the RdRp domain, and we selected those mutated residues predicted to exert greater effect of RPV binding. Since our initial docking calculations predicted three different binding modes for RPV against the RdRp domain (Figures S7–S10), we prioritized the top most critical residues involved in RPV binding for each docking hypotheses. The final list of residues expected to interact with RPV (and possibly with ETR) included F400, K403, N407, K462, Q463, Y477, R483, D665, D666, R731, E735, R739, T796, and W797. All these residues were mutated to alanine and used to experimentally assess the binding of RPV.

Homology Modeling of NS5 Strains
We used the NS5 protein sequence employed in the experimental work (PRVABC59 strain) to build homology models of NS5. Specifically, PDB: 5TMH (MR766 strain) provided the structural template used in the computational work. Models were generated using the protein structure homology-modeling server SWISS-MODEL.[52] Sequence and structure comparisons of NS5 from the two strains show that all 14 mutant residues, used in this study to infer RPV binding, coincide.

We used software programs distributed by Schrödinger[48] for calculations (protein and ligand preparation, binding site detection, molecular docking, ligand conformational search, and mutational analyses), data visualization, and figure preparation.

Determination of Binding Interactions with DSF
DSF or protein thermal shift assays were completed by use of an Applied Biosystems QuantStudio 6 Flex real time PCR instrument with 384-well plate. In these reactions, the assay plates contained a final volume of 20 μL with PBS (10 mM phosphate and 150 mM NaCl [pH 7.4]) and protein samples (purified ZIKV NS5-MBP or MBP) plus the binding partner (RPV) and protein thermal shift Dye kit (cat# 4461146, diluted 1:125 in kit diluent). The plate was sealed and mixed briefly, followed by plate centrifugation at 1,000 rpm for 2 min. After 30-min incubation at 25°C, the plate was then subjected to thermal shift by ramping the temperature from 25°C to 99°C at 0.05°C increments per second. The relative fluorescence emitted by the thermal shift dye was recorded during the temperature ramp phase and plotted versus temperature. The derivative of these thermal melt curves was determined and Tm calculated from these data. The Tm values were plotted as a function of RPV concentration in GraphPad Prism, and the inflection point of the curve determines the binding affinity of ligand to binding protein. The experiments were completed with n = 4–5 replicate samples per treatment. Each experiment was repeated 3–4 times.

Statistical Analysis
All of the values presented on the graphs are given a mean ± SEM. ANOVA and unpaired Student's t test were used to analyze the statistical significance; p values <0.05 were considered statistically significant.

SUPPLEMENTAL INFORMATION

Supplemental Information can be found online at https://doi.org/10.1016/j.ymthe.2019.10.006.

AUTHOR CONTRIBUTIONS

CONFLICTS OF INTEREST

The authors declare no competing interests.

ACKNOWLEDGMENTS

REFERENCES

1. Bogoch, I.I., Brady, O.J., Kraemer, M.U.G., German, M., Creatore, M.I., Kulkarni, M.A., Brownstein, J.S., Mekaru, S.R., Hay, S.I., Groot, E., et al. (2016). Anticipating the international spread of Zika virus from Brazil. Lancet 387, 335–336.

2. Cao-Lormeau, V.M., Roche, C., Teissier, A., Robin, E., Berry, A.L., Mallet, H.P., Sall, A.A., and Musso, D. (2014). Zika virus, French polynesia, South pacific, 2013. Emerg. Infect. Dis. 20, 1085–1086.

3. Haddow, A.D., Schuh, A.J., Yasuda, C.Y., Kasper, M.R., Heang, V., Huy, R., Guzman, H., Tesh, R.B., and Weaver, S.C. (2012). Genetic characterization of Zika virus strains: geographic expansion of the Asian lineage. PLoS Negl. Trop. Dis. 6, e1477.

4. Huang, W.C., Abraham, R., Shim, B.S., Choe, H., and Page, D.T. (2016). Zika virus infection during the period of maximal brain growth causes microcephaly and corticospinal neuron apoptosis in wild type mice. Sci. Rep. 6, 34793.

5. Musso, D., Roche, C., Robin, E., Nhan, T., Teissier, A., and Cao-Lormeau, V.M. (2015a). Potential sexual transmission of Zika virus. Emerg. Infect. Dis. 21, 359–361.

6. Musso, D. (2015b). Zika virus transmission from French Polynesia to Brazil. Emerg. Infect. Dis. 21, 1887.

7. Ventura, C.V., Maia, M., Bravo-Filho, V., Góis, A.L., and Belfort, R., Jr. (2016). Zika virus in Brazil and macular atrophy in a child with microcephaly. Lancet 387, 228.

8. Besnard, M., Lastere, S., Teissier, A., Cao-Lormeau, V., and Musso, D. (2014). Evidence of perinatal transmission of Zika virus, French Polynesia, December 2013 and February 2014. Euro Surveill. 19, 20751.

9. Besnard, M., Eyrolle-Guignot, D., Guillemette-Artur, P., Lastère, S., Bost-Bezeaud, F., Marcelis, L., Abadie, V., Garel, C., Moutard, M.L., Jouannic, J.M., et al. (2016). Congenital cerebral malformations and dysfunction in fetuses and newborns following the 2013 to 2014 Zika virus epidemic in French Polynesia. Euro Surveill. 21, 30181.

10. Culjat, M., Darling, S.E., Nerurkar, V.R., Ching, N., Kumar, M., Min, S.K., Wong, R., Grant, L., and Melish, M.E. (2016). Clinical and Imaging Findings in an Infant With Zika Embryopathy. Clin. Infect. Dis. 63, 805–811.

11. Calvet, G., Aguiar, R.S., Melo, A.S.O., Sampaio, S.A., de Filippis, I., Fabri, A., Araujo, E.S.M., de Sequeira, P.C., de Mendonça, M.C.L., de Oliveira, L., et al. (2016). Detection and sequencing of Zika virus from amniotic fluid of fetuses with microcephaly in Brazil: a case study. Lancet Infect. Dis. 16, 653–660.

12. Chimelli, L., Melo, A.S.O., Avvad-Portari, E., Wiley, C.A., Camacho, A.H.S., Lopes, V.S., Machado, H.N., Andrade, C.V., Dock, D.C.A., Moreira, M.E., et al. (2017). The spectrum of neuropathological changes associated with congenital Zika virus infection. Acta Neuropathol. 133, 983–999.

13. Mlakar, J., Korva, M., Tul, N., Popović, M., Poljšak-Prijatelj, M., Mraz, J., Kolenc, M., Resman Rus, K., Vesnaver Vipotnik, T., Fabjan Vodušek, V., et al. (2016). Zika virus associated with microcephaly. N. Engl. J. Med. 374, 951–958.

14. Lindenbach, B.D., and Rice, C.M. (2003). Molecular biology of flaviviruses. Adv. Virus Res. 59, 23–61.

15. Wang, B., Thurmond, S., Hai, R., and Song, J. (2018). Structure and function of Zika virus NS5 protein: perspectives for drug design. Cell. Mol. Life Sci. 75, 1723–1736.

16. Duan, W., Song, H., Wang, H., Chai, Y., Su, C., Qi, J., Shi, Y., and Gao, G.F. (2017). The crystal structure of Zika virus NS5 reveals conserved drug targets. EMBO J. 36, 919–933.

17. Wang, B., Tan, X.F., Thurmond, S., Zhang, Z.M., Lin, A., Hai, R., and Song, J. (2017). The structure of Zika virus NS5 reveals a conserved domain conformation. Nat. Commun. 8, 14763.

18. Upadhyay, A.K., Cyr, M., Longenecker, K., Tripathi, R., Sun, C., and Kempf, D.J. (2017). Crystal structure of full-length Zika virus NS5 protein reveals a conformation similar to Japanese encephalitis virus NS5. Acta Crystallogr. F Struct. Biol. Commun. 73, 116–122.

19. Halgren, T. (2007). New method for fast and accurate binding-site identification and analysis. Chem. Biol. Drug Des. 69, 146–148.

20. Das, K., Bauman, J.D., Clark, A.D., Jr., Frenkel, Y.V., Lewi, P.J., Shatkin, A.J., Hughes, S.H., and Arnold, E. (2008). High-resolution structures of HIV-1 reverse transcriptase/TMC278 complexes: strategic flexibility explains potency against resistance mutations. Proc. Natl. Acad. Sci. USA 105, 1466–1471.

21. Lansdon, E.B., Brendza, K.M., Hung, M., Wang, R., Mukund, S., Jin, D., Birkus, G., Kutty, N., and Liu, X. (2010). Crystal structures of HIV-1 reverse transcriptase with etravirine (TMC125) and rilpivirine (TMC278): implications for drug design. J. Med. Chem. 53, 4295–4299.

22. Lim, S.P., Noble, C.G., Seh, C.C., Soh, T.S., El Sahili, A., Chan, G.K., Lescar, J., Arora, R., Benson, T., Nilar, S., et al. (2016). Potent allosteric Dengue virus NS5 polymerase inhibitors: mechanism of action and resistance profiling. PLoS Pathog. 12, e1005737.

23. Noble, C.G., Lim, S.P., Chen, Y.L., Liew, C.W., Yap, L., Lescar, J., and Shi, P.Y. (2013). Conformational flexibility of the Dengue virus RNA-dependent RNA polymerase revealed by a complex with an inhibitor. J. Virol. 87, 5291–5295.

24. Noble, C.G., Lim, S.P., Arora, R., Yokokawa, F., Nilar, S., Seh, C.C., Wright, S.K., Benson, T.E., Smith, P.W., and Shi, P.Y. (2016). A conserved pocket in the Dengue virus polymerase identified through fragment-based screening. J. Biol. Chem. 291, 8541–8548.

25. Watts, K.S., Dalal, P., Murphy, R.B., Sherman, W., Friesner, R.A., and Shelley, J.C. (2010). ConfGen: a conformational search method for efficient generation of bioactive conformers. J. Chem. Inf. Model. 50, 534–546.

26. Ericsson, U.B., Hallberg, B.M., Detitta, G.T., Dekker, N., and Nordlund, P. (2006). Thermofluor-based high-throughput stability optimization of proteins for structural studies. Anal. Biochem. 357, 289–298.

27. Niesen, F.H., Berglund, H., and Vedadi, M. (2007). The use of differential scanning fluorimetry to detect ligand interactions that promote protein stability. Nat. Protoc. 2, 2212–2221.

28. Pantoliano, M.W., Petrella, E.C., Kwasnoski, J.D., Lobanov, V.S., Myslik, J., Graf, E., Carver, T., Asel, E., Springer, B.A., Lane, P., and Salemme, F.R. (2001). High-density miniaturized thermal shift assays as a general strategy for drug discovery. J. Biomol. Screen. 6, 429–440.

29. Thammaporn, R., Ishii, K., Yagi-Utsumi, M., Uchiyama, S., Hannongbua, S., and Kato, K. (2016). Mass spectrometric characterization of HIV-1 reverse transcriptase interactions with non-nucleoside reverse transcriptase inhibitors. Biol. Pharm. Bull. 39, 450–454.

30. Lazear, H.M., Govero, J., Smith, A.M., Platt, D.J., Fernandez, E., Miner, J.J., and Diamond, M.S. (2016). A mouse model of Zika virus pathogenesis. Cell Host Microbe 19, 720–730.

31. Dowall, S.D., Graham, V.A., Rayner, E., Atkinson, B., Hall, G., Watson, R.J., Bosworth, A., Bonney, L.C., Kitchen, S., and Hewson, R. (2016). A susceptible mouse model for Zika virus infection. PLoS Negl. Trop. Dis. 10, e0004658.

32. Zukor, K., Wang, H., Siddharthan, V., Julander, J.G., and Morrey, J.D. (2018). Zika virus-induced acute myelitis and motor deficits in adult interferon αβ/γ receptor knockout mice. J. Neurovirol. 24, 273–290.

33. Grant, A., Ponia, S.S., Tripathi, S., Balasubramaniam, V., Miorin, L., Sourisseau, M., Schwarz, M.C., Sánchez-Seco, M.P., Evans, M.J., Best, S.M., and García-Sastre, A. (2016). Zika virus targets human STAT2 to inhibit type 1 interferon signaling. Cell Host Microbe 19, 882–890.

34. Bukrejewska, M., Derewenda, U., Radwanska, M., Engel, D.A., and Derewenda, Z.S. (2017). Crystal structures of the methyltransferase and helicase from the ZIKA 1947 MR766 Uganda strain. Acta Crystallogr. D Struct. Biol. 73, 767–774.

35. Zhang, C., Feng, T., Cheng, J., Li, Y., Yin, X., Zeng, W., Jin, X., Li, Y., Guo, F., and Jin, T. (2017). Structure of the NS5 methyltransferase from Zika virus and implications in inhibitor design. Biochem. Biophys. Res. Commun. 492, 624–630.

36. Coloma, J., Jain, R., Rajashankar, K.R., García-Sastre, A., and Aggarwal, A.K. (2016). Structures of NS5 methyltransferase from Zika virus. Cell Rep. 16, 3097–3102.

37. Chatrin, C., Talapatra, S.K., Canard, B., and Kozielski, F. (2017). The structure of the binary methyltransferase-SAH complex from Zika virus reveals a novel conformation for the mechanism of mRNA capping. Oncotarget 9, 3160–3171.

38. Jain, R., Butler, K.V., Coloma, J., Jin, J., and Aggarwal, A.K. (2017). Development of a S-adenosylmethionine analog that intrudes the RNA-cap binding site of Zika methyltransferase. Sci. Rep. 7, 1632.

39. Zhou, H., Wang, F., Wang, H., Chen, C., Zhang, T., Han, X., Wang, D., Chen, C., Wu, C., Xie, W., et al. (2017). The conformational changes of Zika virus methyltransferase upon converting SAM to SAH. Oncotarget 8, 14830–14834.

40. Zhao, B., Yi, G., Du, F., Chuang, Y.C., Vaughan, R.C., Sankaran, B., Kao, C.C., and Li, P. (2017). Structure and function of the Zika virus full-length NS5 protein. Nat. Commun. 8, 14762.

41. Godoy, A.S., Lima, G.M., Oliveira, K.I., Torres, N.U., Maluf, F.V., Guido, R.V., and Oliva, G. (2017). Crystal structure of Zika virus NS5 RNA-dependent RNA polymerase. Nat. Commun. 8, 14764.

42. Coutard, B., Barral, K., Lichière, J., Selisko, B., Martin, B., Aouadi, W., Lombardia, M.O., Debart, F., Vasseur, J.J., Guillemot, J.C., et al. (2017). Zika virus methyltransferase: structure and functions for drug design perspectives. J. Virol. 91, e02202–e02216.

43. Ferrero, D.S., Ruiz-Arroyo, V.M., Soler, N., Usón, I., Guarné, A., and Verdaguer, N. (2019). Supramolecular arrangement of the full-length Zika virus NS5. PLoS Pathog. 15, e1007656.

44. Sastry, G.M., Adzhigirey, M., Day, T., Annabhimoju, R., and Sherman, W. (2013). Protein and ligand preparation: parameters, protocols, and influence on virtual screening enrichments. J. Comput. Aided Mol. Des. 27, 221–234.

45. Jacobson, M.P., Pincus, D.L., Rapp, C.S., Day, T.J., Honig, B., Shaw, D.E., and Friesner, R.A. (2004). A hierarchical approach to all-atom protein loop prediction. Proteins 55, 351–367.

46. Harder, E., Damm, W., Maple, J., Wu, C., Reboul, M., Xiang, J.Y., Wang, L., Lupyan, D., Dahlgren, M.K., Knight, J.L., et al. (2016). OPLS3: a force field providing broad coverage of drug-like small molecules and proteins. J. Chem. Theory Comput. 12, 281–296.

47. Gianti, E., Messick, T.E., Lieberman, P.M., and Zauhar, R.J. (2016). Computational analysis of EBNA1 "druggability" suggests novel insights for Epstein-Barr virus inhibitor design. J. Comput. Aided Mol. Des. 30, 285–303.

48. Schrödinger Release (2018). 2018-2: LigPrep (New York, NY: Schrödinger, LLC).

49. Shelley, J.C., Cholleti, A., Frye, L.L., Greenwood, J.R., Timlin, M.R., and Uchimaya, M. (2007). Epik: a software program for pK(a) prediction and protonation state generation for drug-like molecules. J. Comput. Aided Mol. Des. 21, 681–691.

50. Friesner, R.A., Banks, J.L., Murphy, R.B., Halgren, T.A., Klicic, J.J., Mainz, D.T., Repasky, M.P., Knoll, E.H., Shelley, M., Perry, J.K., et al. (2004). Glide: a new approach for rapid, accurate docking and scoring. 1. Method and assessment of docking accuracy. J. Med. Chem. 47, 1739–1749.

51. Sherman, W., Beard, H.S., and Farid, R. (2006). Use of an induced fit receptor structure in virtual screening. Chem. Biol. Drug Des. 67, 83–84.

52. Waterhouse, A., Bertoni, M., Bienert, S., Studer, G., Tauriello, G., Gumienny, R., Heer, F.T., de Beer, T.A.P., Rempfer, C., Bordoli, L., et al. (2018). SWISS-MODEL: homology modelling of protein structures and complexes. Nucleic Acids Res. 46 (W1), W296–W303.